ADVANCED MATERIALS
www.advmat.de

Efficient Low-temperature Ammonia Cracking Enabled by Strained Heterostructure Interfaces on Ru-free Catalyst

Pei Xiong, Jiangtong Li, Zhihang Xu, Yashan Lin, Robert David Bennett, Yi Zhang, Wei-Min Tu, Ye Zhu, Yun-Liang Soo, Tai-Sing Wu, and Molly Meng-Jung Li**

Ammonia (NH_3) has emerged as a promising liquid carrier for hydrogen (H_2) storage. However, its widespread adoption in H_2 technology is impeded by the reliance on costly Ru catalysts for low-temperature NH_3 cracking reaction. Here, a strained heterostructure Co@$BaAl_2O_{4-x}$ core@shell catalyst is reported that demonstrates catalytic performance at low reaction temperatures comparable to most Ru-based catalysts. This catalyst exhibits exceptional activity across a range of space velocity conditions, maintaining high conversion rates at 475 to 575 °C and achieving an impressive H_2 production rate of 64.6 mmol H_2 g_{cat}^{-1} min^{-1}. Synchrotron X-ray absorption spectroscopy, synchrotron X-ray diffraction, and kinetic studies are carried out to elucidate the dynamic changes of the strained heterostructure interface of Co-core and $BaAl_2O_{4-x}$-overlayer under catalytic working conditions. The performance enhancement mechanisms are attributed to the tensile strained Co surface encapsulated in the defective $BaAl_2O_{4-x}$, which enhances NH_3 adsorption and facilitates the rate-determining N—H dissociation. Furthermore, the strain release and restoration during NH_3 dehydrogenation enable efficient nitrogen desorption, preventing active site poisoning. This work highlights the effectiveness of lattice strain engineering and the development of synergistic strong metal-support interfaces between active metal nanoparticles and oxide support to boost low-temperature NH_3 cracking.

1. Introduction

Hydrogen (H_2) has received considerable attention as a clean energy source because, in fuel cells, it reacts with oxygen to generate electricity, producing only water as a by-product and achieving higher energy conversion efficiencies compared to traditional fossil fuel-based systems.[1] However, achieving the "H_2 economy" requires safe and cost-effective H_2 storage.[2] In this regard, ammonia (NH_3) is considered a promising H_2 carrier due to its i) well-established production and distribution infrastructure, ii) high volumetric and gravimetric H_2 density, and iii) ability to decompose into CO_x-free H_2.[3]

For energy applications, low-temperature NH_3 decomposition is preferred. Nevertheless, the most efficient low-temperature NH_3 decomposition catalytic systems rely heavily on ruthenium (Ru)-based catalysts,[3a,4] which are costly and limit large-scale implementation.[5] As a result, research has shifted toward alternative catalysts using more abundant non-noble metals such as iron (Fe),[6] cobalt (Co),[5] or nickel (Ni).[7] Among these, Co stands out due to its nitrogen binding energy being close to the optimal range of Ru and its lower susceptibility to poisoning.[8] Therefore, Co-based catalysts have emerged as promising candidates for NH_3 decomposition.[5,9]

However, the low-temperature kinetics of NH_3 decomposition are primarily hindered by inefficient NH_3 adsorption and N—H bond dissociation on Co-based catalysts.[5] While

P. Xiong, J. Li, Z. Xu, Y. Lin, Y. Zhang, Y. Zhu, M. M.-J. Li
Department of Applied Physics
The Hong Kong Polytechnic University
Hong Kong 999077, China
E-mail: molly.li@polyu.edu.hk

P. Xiong
The Institute for Advanced Studies
Wuhan University
Wuhan 430072, China

The ORCID identification number(s) for the author(s) of this article can be found under https://doi.org/10.1002/adma.202502034

DOI: 10.1002/adma.202502034

R. D. Bennett
CSIRO Energy, Clayton Laboratories
Clayton South, VIC 3168, Australia

W.-M. Tu, Y.-L. Soo
Department of Physics
National Tsing Hua University
Hsinchu 30013, Taiwan

Y. Zhu, M. M.-J. Li
Research Institute of Smart Energy (RISE)
The Hong Kong Polytechnic University
Hong Kong 999077, China

T.-S. Wu
National Synchrotron Radiation Research Center
Hsinchu 30076, Taiwan
E-mail: wu.ts@nsrrc.org.tw

most Co-based catalysts demonstrate satisfactory performance only at high temperatures (>600 °C), significant efforts have been directed toward achieving complete hydrogen generation at lower temperatures (<500 °C).[10] Consequently, developing more efficient Co-based catalysts capable of enhancing NH_3 adsorption and facilitating N—H bond dissociation at lower temperatures remains a critical challenge. Innovative catalyst material design strategies are urgently needed to achieve efficient and cost-effective H_2 production from NH_3 decomposition.

Lattice strain engineering has emerged as an effective strategy to enhance catalytic performance by modulating the interactions between active sites and reactants.[11] This approach leverages lattice strain to influence the electronic structure of catalysts, thereby tuning their surface adsorption properties. For example, Jin et al. demonstrated that continuously adjusting the lattice strain of Pt(100) within a range of -5.1% to +5.9% effectively modulated the adsorption strength of reaction intermediates involved in methanol oxidation and H_2 evolution reactions.[12] Similarly, Fan et al. investigated the impact of tensile strain on the adsorption energy of catalysts for nitrate reduction reaction, revealing that introducing tensile strain into Ti_2CO_2 MXene shifted the *d*-band center closer to the Fermi level, thereby improving nitrogen (N_2) adsorption and activation.[13] These findings align with the Sabatier principle, which emphasizes achieving optimal adsorption strength to maximize catalytic efficiency. However, the lattice strain strategy has not yet been explored in thermocatalytic NH_3 cracking.

Building on this concept, introducing lattice strain into Co-based NH_3 decomposition catalysts offers a promising approach for further tuning and optimizing catalytic performance. Nonetheless, lattice strain is not static and may dynamically evolve under reaction conditions, presenting additional challenges in understanding its role in catalytic performance. Real-time analysis of lattice strain evolution during catalytic reactions is therefore essential for elucidating its regulatory effects on reaction pathways, enabled by advancements in in situ and *operando* characterization techniques. Such insights will provide a foundation for designing and optimizing advanced Ru-free catalysts with improved efficiency for NH_3 decomposition.

Herein, we leverage our recently established core@shell catalyst synthesis strategy to fabricate $Co@BaAl_2O_{4-x}$ catalysts with a distinct tensile strain at the heterostructure interface, induced by the strong metal-support interaction (SMSI) effect. This catalyst exhibits exceptional activity for NH_3 decomposition, achieving nearly complete NH_3 conversion at a moderate temperature of 475 to 575 °C and maintaining high efficiency under high flow rate conditions. Comprehensive kinetic analysis and in situ characterizations unveil the critical role of the strained Co and $BaAl_2O_{4-x}$ heterostructure interface in enhancing catalytic performance. The tensile strain at the interface elevates the *d*-band center of Co, thereby strengthening NH_3 adsorption and facilitating N—H bond dissociation through modulating electronic structures. Furthermore, the subsequent release of tensile strain after NH_3 adsorption/activation promotes efficient desorption of reaction products, preventing active site poisoning and ensuring sustained catalytic activity. The elucidation of this unique dynamic strain evolution mechanism at the heterostructure interface provides valuable insights into the influence of lattice strain on catalytic processes. These findings highlight the potential of heterostructure interface engineering to advance NH_3 decomposition catalysis and contribute to the broader development of sustainable and efficient catalyst design strategies in clean energy applications.

2. Results and Discussion

2.1. SMSI Core@Shell Catalyst Composition Optimization for NH_3 Decomposition Reaction

The SMSI effect observed in encapsulated heterostructured catalysts is often associated with outstanding performance. Using our recently developed Tammann temperature-guided SMSI core@shell synthesis strategy,[14] we have synthesized various catalysts with different active metals and promoters, optimizing their performance for NH_3 decomposition. Among these, Co-Ba-Al-O composition exhibits superior activity for the low temperature (<600 °C) range (Figure S1, Supporting Information).[14] Further refinement of the Co-Ba-Al-O catalyst was achieved by adjusting synthesis parameters, including the Ba/Al molar ratio, Co content, calcination temperature, and reduction temperature (Figure S2, Supporting Information). The optimal catalyst was synthesized with a Ba/Al molar ratio of 1/2, ca. 31.6 wt.% Co content, a calcination temperature of 500 °C, and a reduction temperature of 700 °C. Transmission electron microscopy (TEM, **Figure 1a**) characterizations reveals a core@shell heterostructure with an average Co particle size of 14.2 ± 2.7 nm (Figure 1b) and a shell thickness of 3.0 ± 0.1 nm (Figure 1c). See Figure S3 (Supporting Information) for size analysis details. X-ray photoelectron spectroscopy (XPS) analysis confirms the presence of oxygen vacancies in the $BaAl_2O_4$ shell due to its formation under reducing conditions (Figure S4a, Supporting Information),[14] thereby the sample is denoted as $Co@BaAl_2O_{4-x}$. When evaluated for NH_3 decomposition across various temperatures and weight hourly space velocities (WHSVs), $Co@BaAl_2O_{4-x}$ demonstrates exceptional performance, achieving an impressive H_2 production rate of 64.6 mmol H_2 g_{cat}^{-1} min^{-1} at a high WHSV of 60000 mL_{NH3} g_{cat}^{-1} h^{-1} (Figure 1d). Notably, the catalyst maintains nearly complete NH_3 conversions between 475 °C and 575 °C, rivalling the performance of most Ru-based catalysts, which typically required 450 to 550 °C to achieve ~99% NH_3 conversion.[15]

Intriguingly, the scanning transmission electron microscope coupled with electron energy loss spectroscopy (STEM-EELS) analysis of the post-reaction $Co@BaAl_2O_{4-x}$ catalyst reveals a pronounced accumulation of nitrogen species specifically at the core@shell interface (Figure 1e). This observation strongly suggests that NH_3 decomposition predominantly occurs at the interface between the Co core and the $BaAl_2O_{4-x}$ shell, with the oxygen vacancies in the shell ensuring permeability for reactants and facilitating the catalytic process (Figures S5 and S6, Supporting Information). The distinctive core@shell structure creates the unique heterostructure interface between metal Co and $BaAl_2O_{4-x}$ support (will be discussed in the following), which suggests a critical role of the metal support interactions in enhancing the catalytic performance.

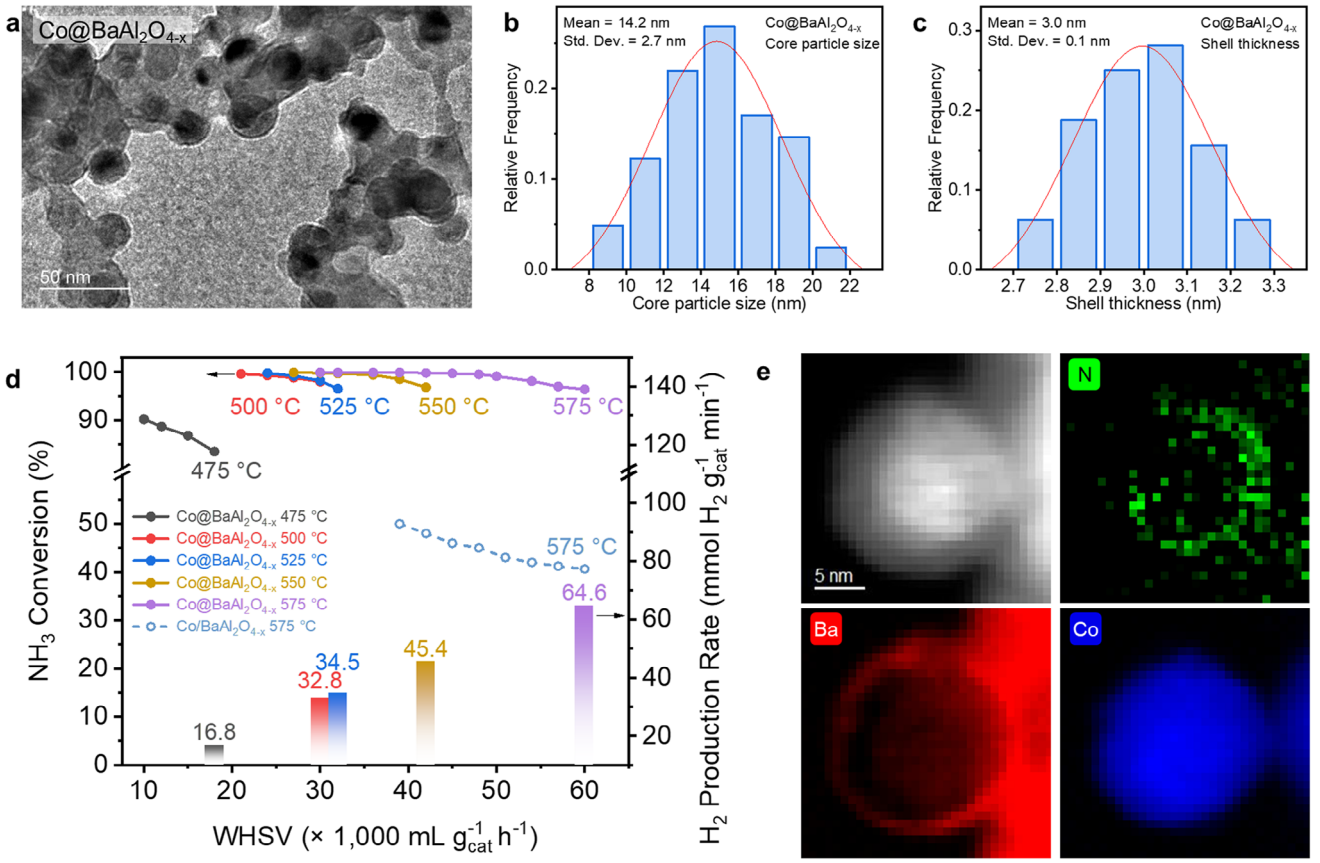

Figure 1. SMSI Core@shell catalyst composition optimization for NH_3 decomposition reaction. a) TEM image of $Co@BaAl_2O_{4-x}$ heterostructure. b) Core particle size distribution of $Co@BaAl_2O_{4-x}$ heterostructure measured from TEM images. c) Shell-thickness distribution of $Co@BaAl_2O_{4-x}$ heterostructure measured from TEM images. d) NH_3 conversion (solid lines) and corresponding H_2 production rate (bar) as a function of WHSV over $Co@BaAl_2O_{4-x}$, as well as $Co/BaAl_2O_{4-x}$ at 575 °C for comparison (dashed line). e) Scanning transmission electron microscopy (STEM) images and electron energy loss spectroscopy (EELS) element distribution maps of post-reaction $Co@BaAl_2O_{4-x}$.

2.2. Improved Reaction Kinetics at the Core@Shell Heterostructure Interface

A series of reaction kinetic studies were conducted to uncover the enhancement mechanism of the $Co@BaAl_2O_{4-x}$ core@shell heterostructure. For comparison, a sample with the same composition but without a core@shell structure, denoted as $Co/BaAl_2O_{4-x}$, was synthesized. Both samples were prepared with a similar size distribution of Co nanoparticles to minimize size effects on catalytic performance (Figure S5e,f; Table S1, Supporting Information).

The catalytic activities of the samples were evaluated for NH_3 decomposition over a temperature range of 200 °C to 650 °C at a WHSV of 30 000 $mL_{NH3}\ g_{cat}^{-1}\ h^{-1}$. The core@shell $Co@BaAl_2O_{4-x}$ catalyst exhibits superior NH_3 conversion compared to the supported $Co/BaAl_2O_{4-x}$ catalyst (Figure S5g, Supporting Information), highlighting the impact of its core@shell heterostructure. The onset temperature for NH_3 decomposition is 200 °C for $Co@BaAl_2O_{4-x}$, compared to 250 °C for $Co/BaAl_2O_{4-x}$. With rising temperature, both catalysts show increasing NH_3 conversion, consistent with the endothermic nature of the reaction. Notably, $Co@BaAl_2O_{4-x}$ achieves near-complete NH_3 conversion at 500 °C, whereas $Co/BaAl_2O_{4-x}$ requires 550 °C to reach thermodynamic equilibrium under identical conditions. Furthermore, the non-core-shell $Co/BaAl_2O_{4-x}$ catalyst displays pronounced susceptibility to high WHSV conditions, with NH_3 conversion decreasing sharply as WHSV increased (Figure 1d), contrasting with the robust performance of the core@shell counterpart.

Arrhenius plots (**Figure 2a**), generated by linearly fitting ln(reaction rate) versus 1/T in the 200–400 °C range (low-conversion regime), reveal distinct apparent activation energies (E_a) for the two catalysts. $Co@BaAl_2O_{4-x}$ exhibits a lower E_a of 64.8 kJ mol^{-1}, comparable to the reported low E_a values for the Ru-based catalysts (ranging from 50 to 130 kJ mol^{-1}),[10b,16] while $Co/BaAl_2O_{4-x}$ shows a much higher E_a of 82.3 kJ mol^{-1}. This reduction in E_a underscores the role of the core@shell heterostructure in facilitating NH_3 decomposition.

Reaction order studies at 350 °C with varying NH_3, H_2, and N_2 concentrations have provided further insights into the catalytic process (see experimental details in the Supporting Information; the results are presented in Figure 2b,c; Figure S7, Supporting Information). As depicted in Figure 2b, the core@shell configuration reduces the positive reaction order for NH_3 from +1.09 ($Co/BaAl_2O_{4-x}$) to +0.78 ($Co@BaAl_2O_{4-x}$). The lower NH_3 order of $Co@BaAl_2O_{4-x}$ indicates that the NH_3 reaction rate

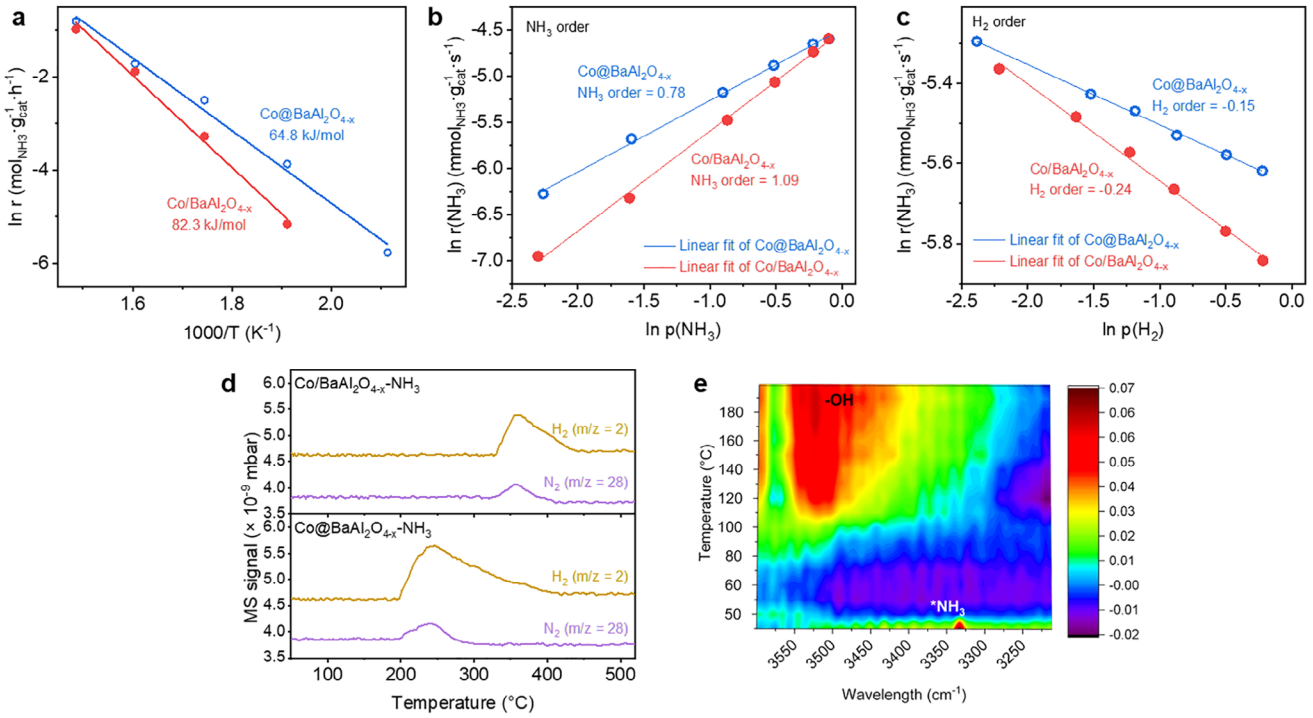

Figure 2. Improved reaction kinetics in the core@shell heterostructure interface. a) E_a determined for the NH_3 decomposition reaction on the Co@$BaAl_2O_{4-x}$ and Co/$BaAl_2O_{4-x}$. b) Reaction orders of NH_3 determined for the NH_3 decomposition reaction at 350 °C on the Co@$BaAl_2O_{4-x}$ and Co/$BaAl_2O_{4-x}$. c) Reaction orders of H_2 determined for the NH_3 decomposition reaction at 350 °C on the Co@$BaAl_2O_{4-x}$ and Co/$BaAl_2O_{4-x}$. d) NH_3-TPSR over the Co@$BaAl_2O_{4-x}$ and Co/$BaAl_2O_{4-x}$. e) Changes in intensity of peaks at 3400–3500 cm^{-1} (-OH species formed at the heterostructured interface) and 3320–3340 cm^{-1} (adsorbed *NH_3 species on Co surface) of in situ diffuse reflectance infrared Fourier transform spectroscopy (DRIFTS experiments with NH_3 adsorption of Co@$BaAl_2O_{4-x}$ from room temperature to 200 °C.

becomes less sensitive to changes in NH_3 concentration. This phenomenon typically occurs when the active sites on the catalyst surface are highly occupied or saturated by NH_3 molecules, suggesting that the structure enhances NH_3 adsorption on active Co sites by alleviating adsorption limitations typically observed in conventional Co catalysts.[3a,5] Additionally, as illustrated in Figure 2c, Co@$BaAl_2O_{4-x}$ displays a less negative H_2 reaction order (−0.15 vs −0.24 for Co/$BaAl_2O_{4-x}$), indicating more efficient hydrogenH removal and reduced hydrogen poisoning during NH_3 dehydrogenation.[3a,17]

NH_3 temperature-programmed surface reaction (NH_3-TPSR) analysis supports the kinetic study findings. After pre-adsorbing NH_3 at 50 °C for 60 min and purging with argon (Ar) (leaving only adsorbed NH_3 on the catalyst surface), temperature ramping reveals higher H_2 and N_2 signal intensities for Co@$BaAl_2O_{4-x}$ compared to Co/$BaAl_2O_{4-x}$ (Figure 2d), confirming core@shell enhances NH_3 adsorption. On the other hand, the in situ diffuse reflectance infrared Fourier transform spectroscopy (DRIFTS) reveals notable -OH peaks during temperature increases, coinciding with the disappearance of adsorbed NH_3 species (see Figure 2e).[3a] These observations indicate N—H bond cleavage during NH_3 dehydrogenation at the heterostructure interface. The H^+ ions from NH_x dehydrogenation on the Co surface bind to $BaAl_2O_{4-x}$ oxygen sites, forming -OH groups.[2]

The above results have demonstrated that the unique SMSI core@shell heterostructure in Co@$BaAl_2O_{4-x}$ enhances key steps in NH_3 decomposition by reducing activation energy, improving NH_3 adsorption, facilitating hydrogen removal, and promoting N—H bond cleavage. This highlights its potential as an efficient catalyst configuration for NH_3 decomposition reactions.

2.3. Identifying Lattice Strain at the Core@Shell Heterostructure Interface

The pronounced enhancement in the catalytic performance of the core@shell heterostructure catalyst has prompted further investigations into its unique structural and electronic properties. **Figure 3a** presents the synchrotron X-ray diffraction (SXRD) patterns of Co@$BaAl_2O_{4-x}$ and Co/$BaAl_2O_{4-x}$, where both samples exhibit distinct crystalline phases of Co and $BaAl_2O_4$. However, a closer examination of the Co(111) diffraction peak reveals notable differences. As shown in Figure 3b, the Co(111) peak in Co@$BaAl_2O_{4-x}$ shifts toward lower angles compared to Co/$BaAl_2O_{4-x}$. This shift indicates an expansion of the Co lattice in the core@shell samples. The refined lattice parameters derived from SXRD, detailed in Table S1 (Supporting Information), confirm this observation by showing that the Co cell volume of Co@$BaAl_2O_{4-x}$ is larger than that of Co/$BaAl_2O_{4-x}$.

To further investigate the lattice characteristics at the Co@$BaAl_2O_{4-x}$ heterostructure interface, AC-STEM was conducted. Figure 3c highlights a selected core@shell particle of Co@$BaAl_2O_{4-x}$, where lattice spacings are measured across three regions extending outward from the core center: area 1

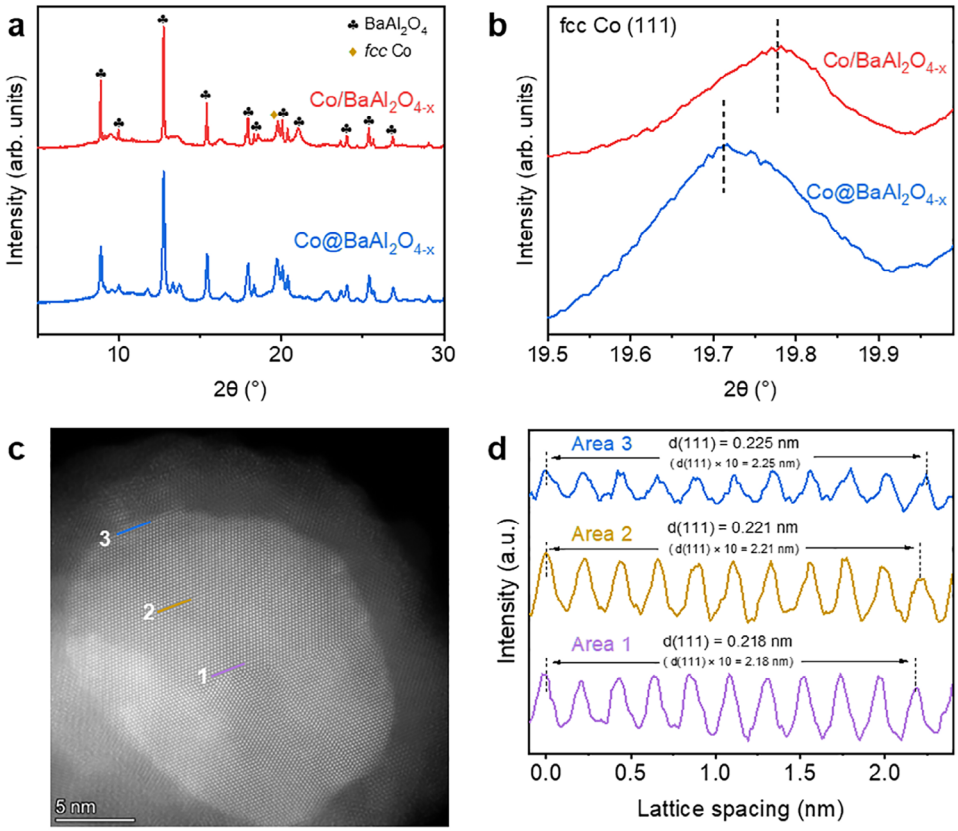

Figure 3. Identifying lattice strain at the core@shell heterostructure interface. a) SXRD patterns of Co@$BaAl_2O_{4-x}$ and Co/$BaAl_2O_{4-x}$ (λ = 0.7000 Å). b) Enlarged views of diffraction peaks of *fcc* Co(111) crystal facet in Co@$BaAl_2O_{4-x}$ and Co/$BaAl_2O_{4-x}$ in Figure 3a. c) Spherical aberration-corrected scanning transmission electron microscopy (AC-STEM) image of the Co@$BaAl_2O_{4-x}$. d) Processed lattice fringe images of areas 1, 2, and 3 in Figure 3c, respectively.

(purple line), area 2 (brown line), and area 3 (blue line). The measured lattice spacings of Co(111) in these regions are 2.18, 2.21, and 2.25 Å, respectively (Figure 3d). The notable increase in lattice spacing observed in area 3 corresponds to a tensile strain of ≈+3.2% relative to the inner core. This direct visualization confirms lattice expansion at the core@shell heterostructure interface.

X-ray absorption spectroscopy (XAS) was conducted to probe the electronic structure of Co in Co@$BaAl_2O_{4-x}$ and Co/$BaAl_2O_{4-x}$ before the reaction. Co K-edge X-ray absorption near-edge structure (XANES) analyses reveal that Co@$BaAl_2O_{4-x}$ exhibits a higher absorption edge position and greater white-line intensity compared to Co/$BaAl_2O_{4-x}$ (**Figure 4a**). Similarly, XPS analysis shows an increase in binding energy for Co 3p

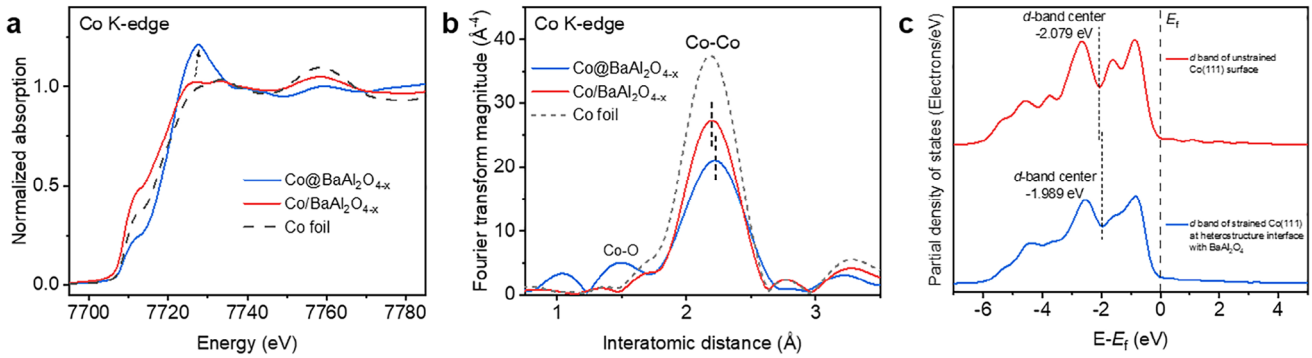

Figure 4. Identifying the electronic structure of Co at the core@shell heterostructure interface. a) Co K-edge XANES spectra of as-synthesized Co@$BaAl_2O_{4-x}$ and Co/$BaAl_2O_{4-x}$, as well as Co foil reference. b) Co K-edge Fourier transformed EXAFS spectra of as-synthesized Co@$BaAl_2O_{4-x}$ and Co/$BaAl_2O_{4-x}$, as well as Co foil reference. c) Projected *d*-band partial density of states of Co atoms in strained Co(111) at the heterostructure interface with $BaAl_2O_4$ and unstrained Co(111) surface.

(Figure S8a, Supporting Information). Further insights are provided by extended X-ray absorption fine structure (EXAFS) spectra, which shows that Co@$BaAl_2O_{4-x}$ has a broader Co—Co peak centered at a longer bond distance compared to Co/$BaAl_2O_{4-x}$ and metallic Co foil. EXAFS fitting results have confirmed the slightly elongated Co—Co bonds in Co@$BaAl_2O_{4-x}$ (Figure 4b; Figure S9; Table S2, Supporting Information). The comprehensive structural and electronic characterizations indicate that tensile strain at the core@shell heterostructure interface induces a higher valence state for Co within the encapsulated configuration.

The observed variation in the valence state of Co can be attributed to the well-established strain-induced *d*-band modification (Figure S10, Supporting Information).[18] The tensile strain experienced by Co in the core@shell heterostructure leads to a reduction in electron density and diminished *d*-band overlap between neighboring Co atoms.[19] These electronic changes, manifested by the higher valence state observed in XAS analysis, result in a narrowing of the *d*-band and a positive shift of its centre to maintain the degree of *d*-band filling.[20] This shift enhances Co's adsorption capacity for the NH_3 molecule,[21] thereby significantly improving the NH_3 decomposition performance of the Co@$BaAl_2O_{4-x}$ catalyst.

To further validate these electronic effects, density functional theory (DFT) simulations were performed. Theoretical models compared the strained Co(111) at the heterostructure interface with $BaAl_2O_4$ to the unstrained Co(111) surface. The partial density of states analysis reveals that the *d*-band center for the strained Co(111) shifts upward by +0.304 eV, bringing it closer to the Fermi level compared to the unstrained surface (Figure 4c). This upward shift aligns with our experimental observations and supports the concept that tensile strain enhances Co's reactivity by facilitating NH_3 adsorption and activation. Details on the construction of DFT models and electronic structure analysis are provided in the Supplementary Information (Figures S11 and S12, Supporting Information). This theoretical evidence complements the experimental results from kinetic studies, providing a critical understanding of the strain-enhanced catalytic performance.

2.4. Dynamic Lattice Strain Release and Restoration in the NH_3 Decomposition Reaction Cycle

The aforementioned findings have provided evidence of the critical role of tensile strain at the core@shell heterostructure interface in enhancing reactant adsorption by modulating electronic structures. To further understand how strain evolves during the NH_3 decomposition reaction, a systematic investigation was conducted using in situ characterization techniques to monitor changes at each reaction step.

Co@$BaAl_2O_{4-x}$ and Co/$BaAl_2O_{4-x}$ samples with pre-adsorbed NH_3 were prepared, denoted as Co@$BaAl_2O_{4-x}$-NH_3 and Co/$BaAl_2O_{4-x}$-NH_3, respectively. XAS analysis reveals that NH_3 adsorption causes the Co—Co peak in the Co K-edge EXAFS of Co@$BaAl_2O_{4-x}$-NH_3 to become narrower and more symmetrical (close to that of Co foil). This contrasts with the broader, asymmetrical peak observed in the strained Co@$BaAl_2O_{4-x}$ (**Figure 5a**; Figure S13; Table S3, Supporting Information). In comparison, no significant changes in Co—Co bond lengths are observed for Co/$BaAl_2O_{4-x}$ upon NH_3 adsorption. Additionally, XANES analysis shows that Co@$BaAl_2O_{4-x}$-NH_3 exhibits a lower absorption edge position and reduced white-line intensity compared to strained Co@$BaAl_2O_{4-x}$ (Figure 5b), indicating strain release and a reduced oxidation state upon NH_3 adsorption.

Interestingly, while literature reports suggest that NH_3 adsorption on transition metal surfaces typically increases the metal's valence state due to interactions with nitrogen species,[22] this trend is observed only for Co/$BaAl_2O_{4-x}$-NH_3. In contrast, the opposite behavior is noted for Co@$BaAl_2O_{4-x}$-NH_3, where strain release induced significant electronic changes. This strain release phenomenon brings adjacent Co atoms closer together, increasing *d*-orbital overlap and causing a downward shift in the *d*-band center. As a result, adsorption strength on the strain-released surface is reduced, which can facilitate the desorption of reaction products.

To demonstrate dynamic strain evolution during the NH_3 decomposition cycle, specifically, strain restoration after product desorption, in situ heating experiments were performed on Co@$BaAl_2O_{4-x}$-NH_3. SXRD monitoring of the Co(111) peak during heating reveals that as pre-adsorbed NH_3 molecules desorb from the surface, the Co(111) peak shifts back toward lower angles (Figure 5c; Figure S14, Supporting Information). At 227 °C (around the H_2 evolution temperature in NH_3-TPSR; Figure 2d), the peak aligns with that of strained Co(111) in clean Co@$BaAl_2O_{4-x}$ at higher temperatures. Complementary in situ XAS measurements shows a gradual increase in Co—Co bond length and valence state during heating, confirming strain restoration as desorption completed (Figure 5d,e; Figure S15; Table S4, Supporting Information).

The dynamic lattice strain evolution mechanism for NH_3 decomposition over the core@shell heterostructured Co@$BaAl_2O_{4-x}$ catalyst is summarized as follows and illustrated in **Figure 6**.

i) Tensile strain formation: At the core@shell heterostructure interface, tensile strain forms and elevates the *d*-band center of Co, enhancing NH_3 adsorption and facilitating its reaction. ii) Strain released upon adsorption: Strain is released when NH_3 adsorbs and reacts on the surface. This strain release shifts the *d*-band downward, reducing adsorption strength and promoting product desorption. iii) Strain restoration after reaction: Following product desorption (e.g., N_2 or H_2), tensile strain at interfacial sites is restored, preparing the catalyst for subsequent reaction cycles.

Such dynamic strain evolution mechanism discovered in this research provides a comprehensive understanding of the interplay between lattice strain, NH_3 adsorption, N—H dissociation, and strain restoration in the core@shell heterostructured Co@$BaAl_2O_{4-x}$ catalyst system. These new mechanistic insights also highlight the importance and effectiveness of strain engineering and interface modulation for enhancing NH_3 decomposition catalysis.

3. Conclusion

In conclusion, this study highlights the dynamic lattice strain evolution mechanism at the interface of core@shell heterostructures during NH_3 decomposition. Employing a core@shell

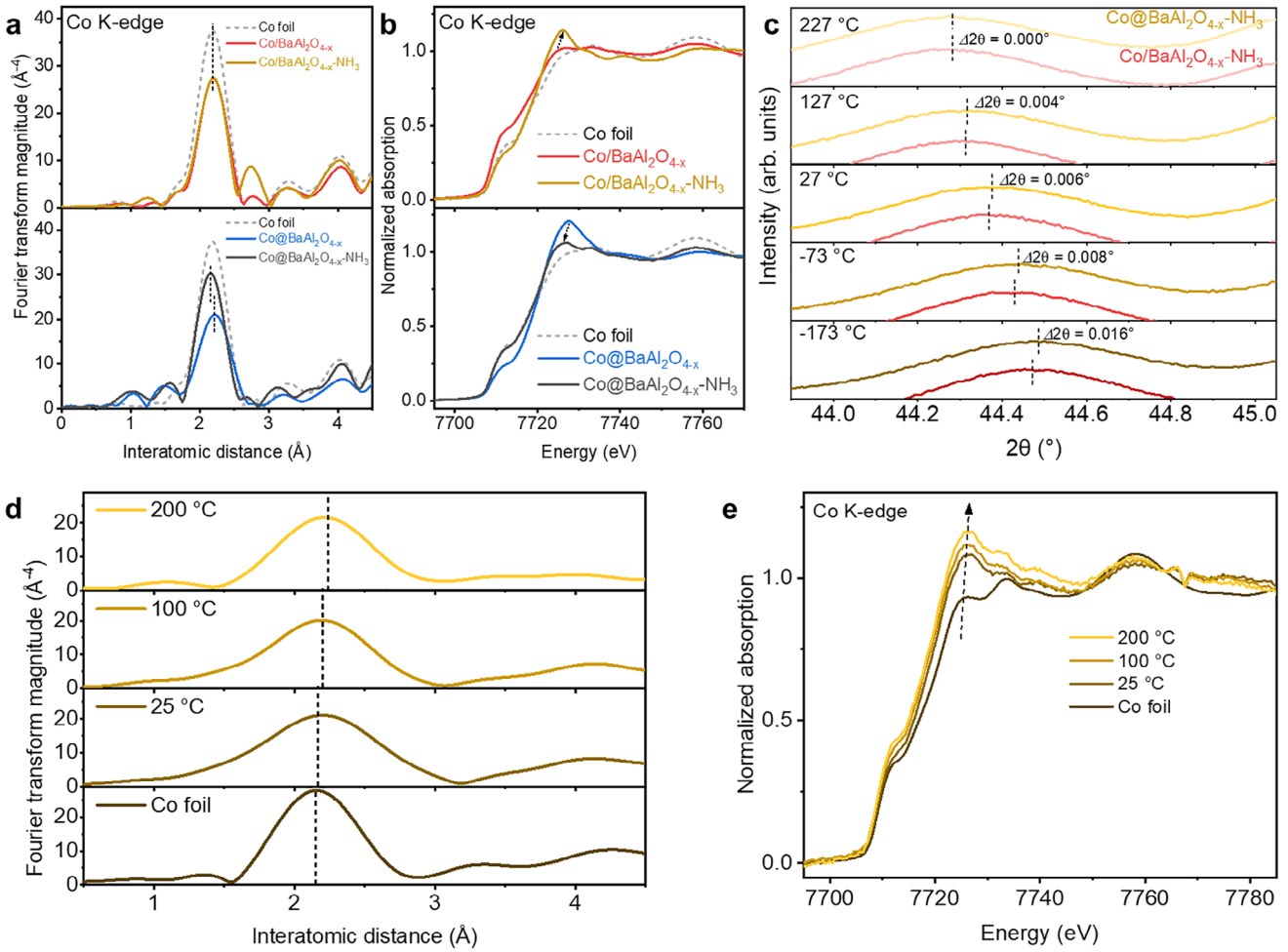

Figure 5. Dynamic lattice strain release and restoration in the NH_3 decomposition reaction cycle. a) Upper panel: Co K-edge Fourier transformed EXAFS spectra of $Co/BaAl_2O_{4-x}$ and $Co/BaAl_2O_{4-x}$-NH_3, as well as Co foil reference; Lower panel: Co K-edge Fourier transformed FT-EXAFS spectra of $Co@BaAl_2O_{4-x}$ and $Co@BaAl_2O_{4-x}$-NH_3, as well as Co foil reference. b) Upper panel: Co K-edge XANES spectra of $Co/BaAl_2O_{4-x}$ and $Co/BaAl_2O_{4-x}$-NH_3, as well as Co foil reference; Lower panel: Co K-edge XANES spectra of $Co@BaAl_2O_{4-x}$ and $Co@BaAl_2O_{4-x}$-NH_3, as well as Co foil reference. c) Enlarged views of diffraction peaks of *fcc* Co(111) crystal facet in in situ SXRD patterns of $Co@BaAl_2O_{4-x}$-NH_3 and $Co/BaAl_2O_{4-x}$-NH_3 with temperature raising from −173 to 227 °C (Full patterns are shown in Figure S14, Supporting Information). d) In situ Co K-edge Fourier transformed FT-EXAFS of $Co@BaAl_2O_{4-x}$-NH_3 under heating from 25 to 200 °C, as well as Co foil reference. e) In situ Co K-edge X-ray absorption near-edge structure (XANES) spectra of $Co@BaAl_2O_{4-x}$-NH_3 under heating at different temperatures, as well as Co foil reference.

catalyst synthesis approach driven by the SMSI effect, we successfully engineered heterostructured interfaces within the Ru-free catalyst formulation, $Co@BaAl_2O_{4-x}$, which operates efficiently under low-temperature reaction conditions. Our findings reveal that the induced lattice strain at the Co core and $BaAl_2O_{4-x}$ overlayer interface modulates the *d*-band center of Co, thereby altering its electronic structure to enhance NH_3 adsorption and facilitate N—H bond dissociation. Furthermore, the release of tensile strain during NH_3 adsorption and activation promotes efficient desorption of reaction products, preventing active site poisoning and ensuring sustained catalytic performance. This dynamic lattice strain evolution mechanism not only facilitates the reaction pathway but also represents a significant advancement in renewable catalysis research, offering promising application opportunities in energy and environmental sustainability.

4. Experimental Section

Preparation Methods for Optimal $Co@BaAl_2O_{4-x}$ and Comparative $Co/BaAl_2O_{4-x}$: The core@shell $Co@BaAl_2O_{4-x}$ catalyst was fabricated through a co-precipitation method with automated pH control, followed by a thermal treatment process. The typical synthesis procedure began by preparing a 50 mL solution containing 0.1 M $Co(NO_3)_2$, 0.05 M $Ba(NO_3)_2$, and 0.1 M $Al(NO_3)_3$ dissolved in deionized (DI) water, maintaining a molar ratio of 2:1:2. At ambient temperature, this mixed-metal solution was added dropwise into a stirred reactor (capacity ranging from 500 mL to 2 L) containing 0.5 M Na_2CO_3 solution. The addition rate of the metal solution was controlled using a syringe pump, with a flow rate typically set between 0.1 and 2.0 mL min^{-1}. To ensure homogeneity, the mixture was stirred vigorously throughout the process. Simultaneously, the pH of the reaction solution was kept stable (pH = 12.5) by gradually introducing 4.0 M NaOH solution via another syringe pump. After all the metal nitrate solutions were completely added, the suspension was aged for 16 h. The resulting mixture was then filtered and rinsed with DI water until the

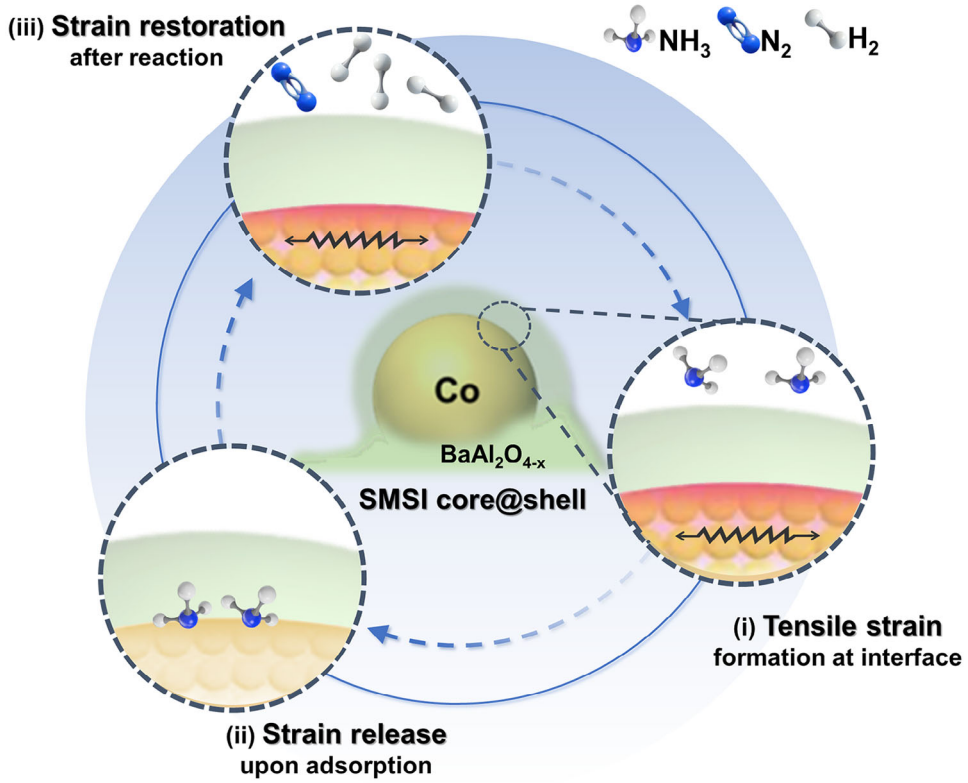

Figure 6. Schematic of the dynamic lattice strain evolution mechanism for NH_3 decomposition over core@shell heterostructured $Co@BaAl_2O_{4-x}$ catalyst.

effluent reached a neutral pH (≈7.0). The collected wet solid was re-dispersed in 200 mL of acetone and stirred at room temperature for 2 h. The resulting solid was vacuum filtered, washed with acetone, and dried overnight in a vacuum oven at room temperature. The dried material was calcined in air at 500 °C for 4 h and subsequently subjected to thermal treatment in a H_2/Ar (5/95, v/v) atmosphere at 700 °C for 2.5 h, which facilitated the formation of the core@shell $Co@BaAl_2O_{4-x}$ catalyst with Co loading of ca. 31.6 wt.%.

In comparison, the $Co/BaAl_2O_{4-x}$ catalyst was synthesized using a wet impregnation method. The synthesis procedure is described as follows: First, the $BaAl_2O_{4-x}$ support was prepared by calcining a mixture of $Ba(NO_3)_2$ and Al_2O_3 directly in a H_2/N_2 (5/95, v/v) atmosphere at 700 °C for 2.5 h. This resulting $BaAl_2O_{4-x}$ support was then combined with an appropriate amount of $Co(NO_3)_2$ in 50 mL of ethanol. The Co content in the $Co/BaAl_2O_{4-x}$ catalyst was adjusted to ≈32.9 wt.%, matching the composition of the $Co@BaAl_2O_{4-x}$ catalyst. The resulting mixture was continuously stirred at 800 rpm for 12 h on a hot plate magnetic stirrer, maintaining a temperature of 50 °C. Following the stirring process, the mixture was transferred to a vacuum oven set at 50 °C for 8 h to remove the ethanol. The dried sample was then calcined in air at 500 °C for 4 h, followed by thermal treatment in a H_2/Ar (5/95, v/v) atmosphere at 700 °C for 2.5 h, ultimately producing the $Co/BaAl_2O_{4-x}$ catalyst.

Material Characterizations: The phases and crystallographic structures of the samples were analyzed using SXRD, conducted on the Powder Diffraction (PD) beamline at the Australian Synchrotron (AS). The measurements were performed with a photon energy of 17.711 keV (wavelength $\lambda = 0.7000$ Å). To investigate the microstructure and phase composition, both STEM in high-angle annular dark field (HAADF) mode and transmission electron microscopy (TEM) were utilized. The analyses were carried out using a double-Cs-corrected STEM (Spectra 300, TFS, USA) and a STEM/TEM instrument (JEM-2100F, JEOL, Japan) integrated with a Gatan Enfina electron spectrometer (USA). X-ray absorption fine structure (XAFS) spectra were collected in fluorescence mode at beamline BL01C of the Taiwan Light Source at the National Synchrotron Radiation Research Center (NSRRC). Photon energy scanning was performed using a Si(111) double crystal monochromator (DCM). In situ XAFS were measured in fluorescence mode using a 19SSD detector at the beamline BL01B1 of the SPring-8 of Japan Synchrotron Radiation Research Institute (JASRI), Hyogo, Japan. Additionally, XPS was conducted using a Thermo Scientific Nexsa instrument, which was equipped with both an electron flood gun and a scanning ion gun. To study surface interactions, in situ DRIFTS experiments were performed on a Bruker FT-IR Spectrometer. The system utilized a high-temperature, high-pressure DRIFTS reaction cell (Harrick Scientific Products Inc.), an MCT/A detector, and measurements were taken at a resolution of 4 cm^{-1}. NH_3-TPSR measurements were conducted by a tube furnace (GSL-1100X, Kejing) combined with a quadrupole mass spectrometer (MS, HPR-20 EGA, Hiden).

More details about Material Characterisations can be found in the Supplementary Information.

Catalytic Performance Evaluation: The catalytic NH_3 decomposition performances were conducted in a fixed-bed flow reactor connected with a mass flow controller (GF 125CXXC, Bronkhorst) to control the flow rate. In a typical experiment, 50 mg of the sieved catalyst sample (45 to 80 mesh) was fixed between the right and left quartz wools at the center of the quartz tube reactor (internal diameter of 4.5 mm), with a thermocouple placed in direct contact with the catalyst bed to monitor the real-time temperature. The packed catalyst was heated to 700 °C at a ramp rate of 5 °C min^{-1} in a flow of 5% H_2/Ar gas with a flow rate of 160 mL min^{-1}, kept at 700 °C for 2.5 h to reduce the catalyst and then exposed to high-purity NH_3 gas (≥99.99%). The WHSV was adjusted to 30000 mL_{NH3} g_{cat}^{-1} h^{-1} by controlling the flow rate. The reaction was then carried out at various temperatures, which increased from 450 to 650 °C in 50 °C increments, and steady-state was allowed to reach before the product analysis by holding each temperature for 60 min. To determine the NH_3 conversions, the

MS equipped with a quadrupole analyzer and a secondary electron multiplier detector operating at 850 eV was used to analyze the composition of the product gas (N_2, H_2, and unreacted NH_3). The accuracy of product analyses was further verified by back titration method, the experimental details of which have been reported in previous studies by our group.[23] The NH_3 conversion (X_{NH3}) were calculated using:

$$X_{NH_3} = \frac{[NH_3]_{inlet} - [NH_3]_{outlet}}{(1 + [NH_3]_{outlet}) \times [NH_3]_{inlet}} \times 100\% \quad (1)$$

where $[NH_3]_{inlet}$ and $[NH_3]_{outlet}$ represent the concentrations of NH_3 measured at the reactor inlet and outlet, respectively.[5] The H_2 production rate, with the unit of mmol H_2 g_{cat}^{-1} min^{-1}, was then calculated based on X_{NH3} by:

$$H_2 \text{ production rate} = \frac{WHSV \times X_{NH_3} \times 1.5}{V_m \times 60} \quad (2)$$

where V_m is the molar volume of gas at standard conditions (24 mL $mmol^{-1}$ at 25 °C and 1 bar).[24]

Kinetic studies were performed across various temperatures and WHSVs to verify that the reaction occurred within the kinetic regime, ensuring no limitations due to mass transfer. The Arrhenius plots and activation energies were calculated using data obtained under similar gas flow rates and compositions, but at different temperatures, while maintaining NH_3 conversion below 30% to avoid equilibrium effects. As such, the activity measurements were conducted under steady-state conditions controlled by reaction kinetics. All catalysts were tested twice to confirm the reproducibility of the results.

Reaction orders were determined by independently varying the concentrations of NH_3, H_2, or N_2 while maintaining Ar as the balance gas. These experiments were performed at 350 °C with a total gas flow rate of 25 mL min^{-1} at atmospheric pressure. For NH_3, its concentration was adjusted between 10% and 90%, with Ar as the balance gas. When determining the reaction order for H_2, the concentration of NH_3 was fixed at 20%, while H_2 was varied between 10% and 80% with Ar as the balance gas. Similarly, for N_2, the NH_3 concentration remained constant at 20%, while N_2 was adjusted within the same range and balanced by Ar.

First-principles Calculations: First-principles calculations were carried out using the pseudopotential plane wave method based on DFT.[25] These computations were performed with the Cambridge Serial Total Energy Package (CASTEP) software.[26] The Perdew-Burke-Ernzerhof (PBE) functional within the generalized gradient approximation (GGA) framework was used to compute the exchange-correlation energy.[27] A cutoff energy of 400 eV was applied for the plane wave basis set.

The geometry of the Co(111)@$BaAl_2O_4$(202) interface was optimized using the Limited Memory Broyden-Fletcher-Goldfarb-Shanno (LBFGS) algorithm.[28] The convergence criteria for interatomic forces, internal stress, atomic displacements, and energy per atom between iterations were set to 0.05 eV $Å^{-1}$, 0.1 GPa, 0.002 Å, and 2.0×10^{-5} eV $atom^{-1}$, respectively. The Brillouin zone was sampled using a $2 \times 5 \times 1$ Monkhorst-Pack grid. Energy calculations were performed in reciprocal space to determine the total energy.

The *d*-band centers for majority and minority spin states were calculated using the first moment of the density of states (DOS). The *d*-band center was obtained using the Equation (3):[29]

$$\varepsilon_{d\sigma} = \frac{\int_{-\infty}^{\infty} ED_{d\sigma}(E - E_F)\,dE}{\int_{-\infty}^{\infty} D_{d\sigma}(E - E_F)\,dE} \quad (3)$$

here, $D_{d\sigma}(E)$ represents the projected DOS of the transition metal's *d*-states for spin σ, and E_F is the Fermi energy of the system. Spin-dependent fractional occupations were calculated using the following Equation (4):

$$f_\sigma = \frac{\int_{-\infty}^{E_F} D_{d\sigma}(E)\,dE}{5} \quad (4)$$

Statistical Analysis: The MS data was detected using the MASsoft 10 Professional. The SXRD data were treated using the program PDViPeR. The XANES data were background-subtracted and normalized using the AUTOBK routine in Athena software. An established data reduction method was used to extract the EXAFS χ-functions from the raw experimental data using the IFEFFIT software. The XPS data were processed by Computer aided surface analysis for X-ray photoelectron spectroscopy (CasaXPS) software and the carbon 1s peak at 284.6 eV was used to calibrate all the spectra. The core particle size and shell thickness of catalysts were measured using TEM images with the help of Ganta DigitalMicrograph and Nano measurer softwares. All the figures were formatted in Origin. Details can be found in the "III. Material characterizations" of the Supporting Information.

Supporting Information

Supporting Information is available from the Wiley Online Library or from the author.

Acknowledgements

The authors thank Dr Anita D'Angelo and the Powder Diffraction (PD) beamline at Australian Synchrotron, Melbourne, Australia. The authors thank the beamline BL01C at the National Synchrotron Radiation Center, Hsinchu, Taiwan. The authors thank the beamline BL01B1 at the SPring-8 of the Japan Synchrotron Radiation Research Institute, Hyogo, Japan.The work described in this paper was substantially supported by the grants from the Research Grants Council of the Hong Kong Special Administrative Region, China (Project No. PolyU15221924 and PolyU15309424, as well as Environment and Conservation Fund – Research and Development Projects (ECF 33/2022) and the Green Tech Fund (GTF202220122) from the Environment and Ecology Bureau of Hong Kong. P.X. also acknowledges the support from the Postdoctoral Fellowship Program of CPSF under Grant Number GZC20241255, the Postdoctoral General Fund of CPSF under Grant Number 2024M762475, and the Hubei Province Postdoctoral Talent Introduction Project (2024HBBHJD078).

Conflict of Interest

The authors declare no conflict of interest.

Data Availability Statement

The data that support the findings of this study are available from the corresponding author upon reasonable request.

Keywords

ammonia cracking, core@shell catalysts, dynamic strain evolution, heterostructure interface, lattice strain

Received: January 29, 2025
Revised: April 10, 2025
Published online:

[1] K. Nagaoka, T. Eboshi, Y. Takeishi, R. Tasaki, K. Honda, K. Imamura, K. Sato, *Sci. Adv.* **2017**, *3*, 1602747.
[2] K. C. Leung, S. Hong, G. Li, Y. Xing, B. K. Y. Ng, P. L. Ho, D. Ye, P. Zhao, E. Tan, O. Safonova, T. S. Wu, M. M. Li, G. Mpourmpakis, S. C. E. Tsang, *J. Am. Chem. Soc.* **2023**, *145*, 14548.

[3] a) H. Fang, S. Wu, T. Ayvali, J. Zheng, J. Fellowes, P. L. Ho, K. C. Leung, A. Large, G. Held, R. Kato, K. Suenaga, Y. I. A. Reyes, H. V. Thang, H. T. Chen, S. C. E. Tsang, *Nat. Commun.* **2023**, *14*, 647; b) F. Schüth, R. Palkovits, R. Schlögl, D. S. Su, *Energy Environ. Sci.* **2012**, *5*, 6278.
[4] J. Cha, T. Lee, Y.-J. Lee, H. Jeong, Y. S. Jo, Y. Kim, S. W. Nam, J. Han, K. B. Lee, C. W. Yoon, H. Sohn, *Appl. Catal. B Environ.* **2021**, *283*, 119627.
[5] a) P. Xie, Y. Yao, Z. Huang, Z. Liu, J. Zhang, T. Li, G. Wang, R. Shahbazian-Yassar, L. Hu, C. Wang, *Nat. Commun.* **2019**, *10*, 4011. b) S. A. Beck, J. Marlowe, M. J. Gordon, P. Christopher, *J. Phys. Chem. C* **2024**, *128*, 8590.
[6] L. Huo, B. Liu, H. Li, B. Cao, X.-c. Hu, X.-p. Fu, C. Jia, J. Zhang, *Appl. Catal. B Environ.* **2019**, *253*, 121.
[7] K. Ogasawara, T. Nakao, K. Kishida, T.-N. Ye, Y. Lu, H. Abe, Y. Niwa, M. Sasase, M. Kitano, H. Hosono, *ACS Catal.* **2021**, *11*, 11005.
[8] a) Y. Jiang, R. Takashima, T. Nakao, M. Miyazaki, Y. Lu, M. Sasase, Y. Niwa, H. Abe, M. Kitano, H. Hosono, *J. Am. Chem. Soc.* **2023**, *145*, 10669; b) Z. Lendzion-Bielun, U. Narkiewicz, W. Arabczyk, *Materials* **2013**, *6*, 2400.
[9] a) Z. Li, Y. Lu, J. Li, M. Xu, Y. Qi, S. W. Park, M. Kitano, H. Hosono, J. S. Chen, T. N. Ye, *Nat. Commun.* **2023**, *14*, 6373; b) Y. Zhu, H. Pan, Q. Li, X. Huang, W. Xi, H. Tang, W. Tu, S. Wang, H. Tang, H. Zhang, *Adv. Sci.* **2024**, *11*, 2406659; c) K. Xu, Y. Y. Zhang, W. W. Wang, M. Peng, J. C. Liu, C. Ma, Y. W. Zhang, C. J. Jia, D. Ma, C. H. Yan, *Angew. Chem., Int. Ed.* **2025**, *64*, 202416195; d) A. Gunnarson, A. Cao, O. F. Sloth, M. Varón, R. Bueno Villoro, T. Veile, C. D. Damsgaard, C. Frandsen, J. K. Nørskov, I. Chorkendorff, *Energy Environ. Sci.* **2024**, *17*, 9313.
[10] a) G. Thomas, G. Parks, *Potential Roles of Ammonia in a Hydrogen Economy*, U.S. Department of Energy, Washington, DC **2006**; b) S. Mukherjee, S. V. Devaguptapu, A. Sviripa, C. R. F. Lund, G. Wu, *Appl. Catal. B Environ.* **2018**, *226*, 162.
[11] a) W. Cheng, X. Zhao, H. Su, F. Tang, W. Che, H. Zhang, Q. Liu, *Nat. Energy* **2019**, *4*, 115; b) M. Luo, S. Guo, *Nat. Rev. Mater.* **2017**, *2*, 17059.
[12] T. He, W. Wang, F. Shi, X. Yang, X. Li, J. Wu, Y. Yin, M. Jin, *Nature* **2021**, *598*, 76.
[13] Y. Zhang, Y. Wang, N. Ma, B. Liang, Y. Xiong, J. Fan, *Small* **2024**, *20*, 2306840.
[14] P. Xiong, Z. Xu, T. S. Wu, T. Yang, Q. Lei, J. Li, G. Li, M. Yang, Y. L. Soo, R. D. Bennett, S. P. Lau, S. C. E. Tsang, Y. Zhu, M. M. Li, *Nat. Commun.* **2024**, *15*, 420.
[15] a) C. Chen, K. Wu, H. Ren, C. Zhou, Y. Luo, L. Lin, C. Au, L. Jiang, *Energy Fuel.* **2021**, *35*, 11693; b) K. E. Lamb, M. D. Dolan, D. F. Kennedy, *Int. J. Hydrogen. Energy* **2019**, *44*, 3580; c) F. Chang, W. Gao, J. Guo, P. Chen, *Adv. Mater.* **2021**, *33*, 2005721.
[16] a) X. Ju, L. Liu, P. Yu, J. Guo, X. Zhang, T. He, G. Wu, P. Chen, *Appl. Catal. B Environ.* **2017**, *211*, 167; b) A. M. Karim, V. Prasad, G. Mpourmpakis, W. W. Lonergan, A. I. Frenkel, J. G. Chen, D. G. Vlachos, *J. Am. Chem. Soc.* **2009**, *131*, 12230.
[17] N. Morlanés, S. Sayas, G. Shterk, S. P. Katikaneni, A. Harale, B. Solami, J. Gascon, *Catal. Sci. Technol.* **2021**, *11*, 3014.
[18] Q. Hu, K. Gao, X. Wang, H. Zheng, J. Cao, L. Mi, Q. Huo, H. Yang, J. Liu, C. He, *Nat. Commun.* **2022**, *13*, 3958.
[19] B. Hu, Y. Xie, Y. Yang, J. Meng, J. Cai, C. Chen, D. Yu, X. Zhou, *Appl. Catal. B Environ.* **2023**, *324*, 122257.
[20] L. Wang, Z. Zeng, W. Gao, T. Maxson, D. Raciti, M. Giroux, X. Pan, C. Wang, J. Greeley, *Science* **2019**, *363*, 870.
[21] B. You, M. T. Tang, C. Tsai, F. Abild-Pedersen, X. Zheng, H. Li, *Adv. Mater.* **2019**, *31*, 1807001.
[22] K. G. Kirste, S. Laassiri, Z. Hu, D. Stoian, L. Torrente-Murciano, J. S. J. Hargreaves, K. Mathisen, *Phys. Chem. Chem. Phys.* **2020**, *22*, 18932.
[23] L. Zhai, C. S. Wong, H. Zhang, P. Xiong, X. Xue, Y. L. Ho, C. Xu, Y. C. Fong, J. Mei, W. W. Chan, S. C. Ip, S. Niu, S. P. Lau, K. W. E. Cheng, M. M.-J. Li, *Chem. Eng. J.* **2023**, *452*, 139390.
[24] X. Zhang, L. Liu, J. Feng, X. Ju, J. Wang, T. He, P. Chen, *Catal. Lett.* **2022**, *152*, 1170.
[25] V. Milman, K. Refson, S. J. Clark, C. J. Pickard, J. R. Yates, S. P. Gao, P. J. Hasnip, M. I. J. Probert, A. Perlov, M. D. Segall, *J. Mol. Struct. THEOCHEM* **2010**, *954*, 22.
[26] S. J. Clark, M. D. Segall, C. J. Pickard, P. J. Hasnip, M. I. J. Probert, K. Refson, M. C. Payne, *Z. Krist.-Cryst. Mater.* **2005**, *220*, 567.
[27] G. Kresse, J. Hafner, *J. Phys. Condens. Matter* **1994**, *6*, 8245.
[28] a) A. Sherman, *J. Electrochem. Soc.* **1992**, *137*, 1892; b) T. H. Fischer, J. Almlof, *J. Phys. Chem.* **1992**, *96*, 9768.
[29] S. Bhattacharjee, U. V. Waghmare, S. C. Lee, *Sci. Rep.* **2016**, *6*, 35916.